THE JOURNAL OF PHYSICAL CHEMISTRY C

Article

pubs.acs.org/JPCC

In Situ Exploration of Thermal-Induced Domain Evolution with Phase Transition in $LiNbO_3$-Modified $K_{0.5}Na_{0.5}NbO_3$ Single Crystal

Anyang Cui,[†] Kai Jiang,[†] Peng Zhang,[†] Liping Xu,[†] Guisheng Xu,[‡] Xiaomin Chen,[§] Zhigao Hu,*[,†] and Junhao Chu[†]

[†]Key Laboratory of Polar Materials and Devices (MOE) and Technical Center for Multifunctional Magneto-Optical Spectroscopy (Shanghai), Department of Electronic Engineering, East China Normal University, Shanghai 200241, China

[‡]Key Laboratory of Transparent Opto-Functional Advanced Inorganic Materials, Shanghai Institute of Ceramics, Chinese Academy of Sciences, Shanghai 201899, China

[§]Bruker (Beijing) Scientific Technology Co., Ltd., Beijing 100081, China

ABSTRACT: Temperature dependent domain evolution and domain-wall motion of ferroelectric materials have attracted dramatically increased interest due to the crucial influences on piezo- and dielectric properties and the performances of related nanoapplications. Here, the unambiguous evolutions of 90°/180° domain walls accompanied by phase transition have been discovered first in $LiNbO_3$ doped $(K_{0.5}Na_{0.5})NbO_3$ single crystal during heating and cooling processes by *in situ* coupling characterizations of Raman spectra and piezoresponse force microscopy (PFM). Considering the vibrational modes of a NbO_6 octahedron, the stretching modes of $A_{1g}(\nu_1)$, $E_g(\nu_2)$, and the bending mode $F_{2g}(\nu_5)$ are sensitive to structural transition as well as the diversity of domain evolution. These modes are used to discuss the formation of 60° domain walls and the change of 90° domain-wall density. Under the precise control of the temperature gradient, homogeneous striped 90° domain boundaries movement and microscale out-of-plane polarization reversal can be observed. Simultaneously, as one of the most distinctive features from the ferroelectric first-order phase transition, a thermal hysteresis effect has been found in $(K_{0.5}Na_{0.5})NbO_3$−$0.05LiNbO_3$ single crystal. The present study focuses on the correlation of crystal structural transformation and thermal domain evolution. It affords an effective opportunity to explore the stable performance in a broad temperature range for domain-wall dependent ferroelectric devices.

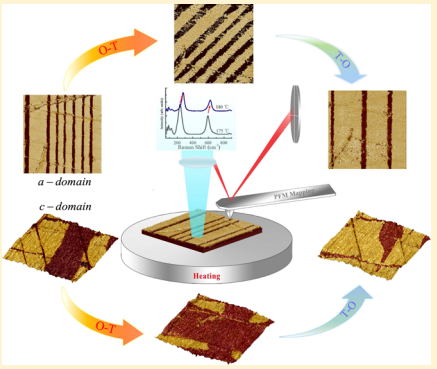

1. INTRODUCTION

Oxide functional materials have been widely applied into electric-optic devices and nanoelectronics such as ferroelectric nonvolatile memories. Storing a data bit means enlarging the size of one nanoscale polar region by the movement of a domain boundary in ferroelectrics.[1−3] Advanced research studies have paid more attention to domain engineering by electrical, mechanical, and optical controls.[3−6] Simultaneously, the piezoelectric and dielectric properties of ferroelectric materials are generally attributed to domain evolution and domain-wall movement.[7] With rapid development and widespread applications of electronic devices, ferroelectric thermal stability plays a crucial role in the working performances at the condition of being away from room temperature (RT). In past decades, research studies on temperature dependent domain engineering were not as frequent as those on macroscopic ferroelectricity. Thus, to better understand and further enhance ferroelectric responses, domain evolution during heating and cooling cycles must be studied. For illustrating domain structure and distribution, many techniques have been employed including transmission electron microscopy (TEM),[8] optical microscopy (OM),[9,10] backscattered mode scanning electron microscopy (BM-SEM),[9,11,12] and piezoresponse force microscopy (PFM).[4,5,7,13] The skillful *in situ* combination with Raman spectra or Raman mapping will make the discussion between domains and crystal structures more fascinating.[14,15]

Moreover, $Pb(Zr_{1-x}Ti_x)O_3$ (PZT) and other related modified materials have become one of the main components in commercial products such as high-performance piezoelectric sensors depending on their excellent piezo- and dielectric responses.[7,16] However, with the environment-friendly development in consideration, lead-free ferroelectric materials have attracted much attention in recent years. One of the most promising alternative candidates is doped $(K_{0.5}Na_{0.5})NbO_3$ (KNN)-based ferroelectrics. In previous works, the property improvements of the KNN system have made great progress through compositional modification, for example, including the dopants of Mn, Ta, Li, and Sb; procedure control of material fabrication; and so on.[17−25] Some pioneering research from Wu et al. found the giant d_{33} (~490 pC/N), high Curie temperature (T_C ~ 335 °C), and high strain in alkali-niobate-based ceramics,

Received: April 8, 2017
Revised: May 28, 2017
Published: June 12, 2017

DOI: 10.1021/acs.jpcc.7b03325
J. Phys. Chem. C 2017, 121, 14322−14329

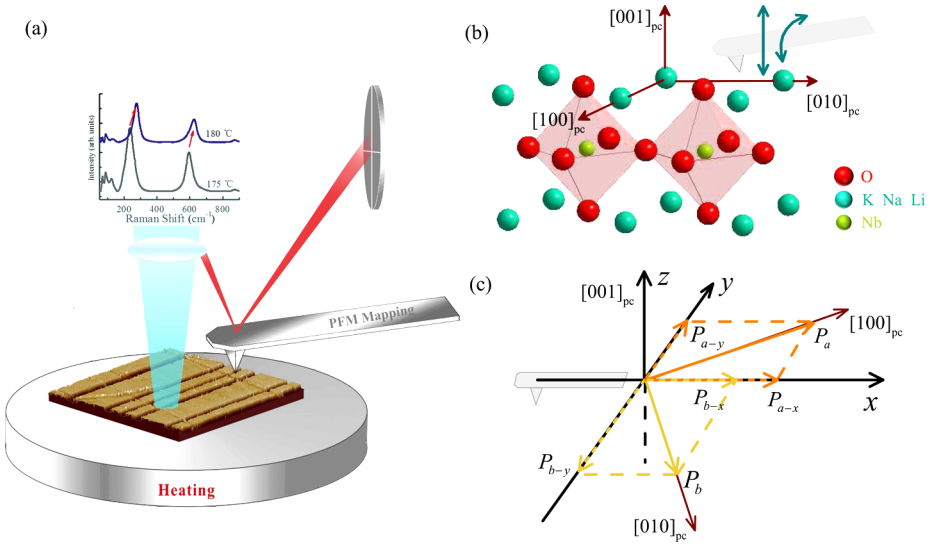

Figure 1. (a) Experimental setup of *in situ* characterizations of Raman spectra and PFM. A 30 × 30 μm^2 IP domain image is incorporated into a three-dimensional schematic drawing showing the experimental configuration. The 488 nm excitation laser for Raman spectra is shown in blue and the AFM internal detection laser in red. The stage can be used to heat or cool samples as well as control the same observed site by *in situ* PFM and Raman spectra. (b) Lattice structure of KNN-LN with pseudocubic indices, and the working principles of PFM for getting OP and IP domains (vertical and torsional double-direction dark-cyan arrow, respectively) based on AFM tip. (c) The mechanism of analyzing IP 90° domains depending on the method of rotating sample. Axis *x* is the tip scanning direction. $\mathbf{P}_a$ (orange) and $\mathbf{P}_b$ (yellow) are the real in-plane polarized directions, and their *x*- and *y*-components are marked as $\mathbf{P}_{a/b-x/y}$ in dotted lines. Pseudocubic lattice indices correspond to structures in part b.

because of the construction of an R−T phase boundary as well as superior ferroelectric responses.[25,26] Meanwhile, a polymorphic phase transition (PPT) between tetragonal (T) and orthorhombic (O) phases exists in the KNN-based system, which is found in some perovskite materials such as $BaTiO_3$. This suggests that the improvement of properties is related to decreasing the O−T polymorphic phase transition point (T_{O-T}) to RT,[27] but the drawback of temperature sensitivity from PPT makes KNN-based materials limited for further applications. Recently, the breakthrough has been reported by Wang et al. in the temperature insensitivity of electric-field-induced strain behavior in 0.95(Na, K, Li)(Nb, Ta)O_3−0.05$CaZrO_3$ piezoceramics, which extends the transition range between T and O phases under an *E*-field.[19,28] By contrast, studies on thermal-field-induced domain evolution and domain engineering of KNN-based ferroelectrics lag behind. Therefore, it is necessary to discuss the relationship among different phase structures, thermal stability, and ferroelectric domains for the future development of KNN related applications.

To demonstrate the domain structures and evolutions that accompanied the phase transition in ferroelectric materials, we focus on the composition-graded 0.95($K_{0.5}Na_{0.5}$)NbO_3−0.05$LiNbO_3$ (KNN-LN) single crystal with excellent piezoelectric properties. The phase transition from the O to T phase occurs in the range 175−180 °C with increasing temperature, whereas transformation from T to O occurs within 165−175 °C during the cooling process. As one of the specialties of ferroelectric first-order phase transition, thermal hysteresis has been indicated by analyzing temperature dependent Raman spectra. At the same time, *in situ* atomic force microscopy (AFM) was realized to investigate the domain evolution in heating and cooling cycles from 20 to 240 °C. Out-of-plane (OP) *c*-domains, in-plane (IP) *a*-domains, and polarization reversal have been clearly observed via PFM. Intrinsic evolution mechanism of the 60° and 90° domain walls was discussed in the O phase by the change of Raman-active optical modes. Coupling the results of PFM and Raman spectra may provide a crucial clue for understanding the piezoelectric response and domain stability for the KNN-LN crystal in a certain temperature range as well as domain engineering for future ferroelectric applications.

2. EXPERIMENTAL SECTION

2.1. Growth of KNN-LN Crystal. Various approaches have been taken to prepare pure and doped KNN single crystals in recent years such as the floating zone method (FZM),[18] the flux-Bridgman method,[27] top-seeded solution growth (TSSG) method,[29] and solid state crystal growth (SSCG) method.[30] In our work, 0.95($K_{0.5}Na_{0.5}$)NbO_3−0.05$LiNbO_3$ was grown by the flux-Bridgman method.[31] The raw materials were high-purity (up to 99.99%) powders consisting of Na_2CO_3, K_2CO_3, Li_2CO_3, and Nb_2O_5. Standard stoichiometric powders were mixed thoroughly. Then, mixed powders were calcined in air at 800 °C for 2 h, KCL−K_2CO_3 (molar ratio of 0.634:0.366) flux was added to the calcined powders in 1:4 by weight, and mixtures were pressed at cold isostatic conditions of 200 MPa. The samples were charged in platinum crucibles (held at 1200 °C for over 10 h, and then decreased at a rate of 0.2−0.4 mm/h), which were sealed to suppress the volatilization of melts. In the growth furnace, a temperature gradient of 30−50 °C was applied near the solid−liquid interface. After the crystal growth, cooling treatment with the rate of 100−200 °C per hour to RT was applied to the growth furnace. The crystal blank was washed using distilled water to get (001)-cut KNN-LN crystal. In order to eliminate the surface overlayer artifacts in Raman scattering and PFM experiments, the sample was single-side polished along the [001] direction with mechanical polish. For modifying the internal stress before a series of experiments, a KNN-LN single crystal was processed at a low temperature of about −180 °C for 5 min and then returned back to RT.

2.2. Optical and AFM Characterizations. Raman spectra were obtained through a Jobin-Yvon LabRAM HR 800 micro-

DOI: 10.1021/acs.jpcc.7b03325
J. Phys. Chem. C 2017, 121, 14322−14329

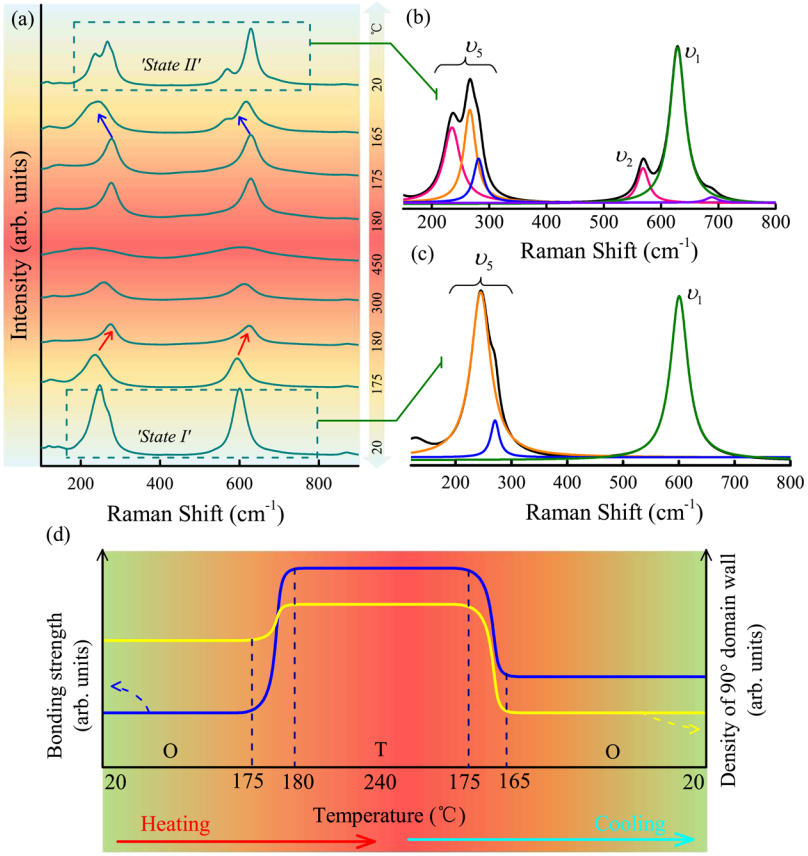

Figure 2. (a) Temperature dependent Raman spectra collected from 20 to 450 °C with heating and cooling cycles. (b, c) Magnified Raman spectra from the dotted rectangular areas and Lorentzian fittings related with state I and state II. (d) General trends of bonding strength and density of 90° domain wall with successive O−T−O phase transition.

Raman spectrometer. A 50× microscope with a working distance of 18 mm and the exciting laser with the wavelength of 488 nm were applied. The spectral resolution is better than 1 cm^{-1}. Laser power focusing on the sample is about 4 mW, so the heating effect from the laser beam can be ignored. The Raman scattering signals were collected by an air-cooled charge coupled device with 1800 grooves/mm grating in the frequency range 50−1000 cm^{-1}. For the sake of comparison and for removal of the contribution from the Bose−Einstein population factor, Raman data were corrected by the Bose−Einstein temperature factor. In addition, sample topographies and ferroelectric domains were investigated via an atomic force microscope (AFM, Dimension Icon, Bruker) with a conductive probe (DDESP-V2, the doped diamond coating, tip radius ≈100 nm) in contact mode. An ac tip bias (15 kHz, 4000 mV) was applied here. The Dimension heater/cooler could heat or cool the sample from 20 to 240 °C with accuracy of 1 °C. *In situ* characterizations with AFM and Raman spectra were realized by a Piezo XY-Nanopositioning Stage [Physik Instrumente (PI)] equipped with a heater/cooler stage (Dimension Icon, Bruker). For ensuring the internal stress's evolution and stability of a KNN-LN crystal, all thermal cycles during heating and cooling were controlled at the rate of 10 °C/min with temperature plateaus of 10 min for AFM and Raman spectra.

3. RESULTS AND DISCUSSION

3.1. Experimental Configuration. In order to demonstrate the relation of crystal structure and domain evolution, we design a kit of the experimental configuration for *in situ* measurements, shown in Figure 1a. Raman spectra were used to study the O−T phase transition temperature (T_{O-T}) and analyze the NbO_6 octahedron distortion, which was induced by internal stress related with the evolution of 60°/90° domain walls in the KNN-LN single crystal. AFM was employed to image the topography, the OP *c*-domain, and IP *a*-domain through adding an ac tip bias. The tip motion for obtaining domain images is illustrated in Figure 1b, which includes a scheme of the lattice structure of KNN-LN with pseudocubic axes. In this work, a method of rotating a sample was taken to map the same zone to obtain the polarization orientations of *a*-domain.[32,33] The interfacial polarization angles were determined by having the angle resolved, as shown in Figure 1c. The AFM probe scanning direction is along axis *x*. $\mathbf{P}_a$ and $\mathbf{P}_b$ are actual polarization vectors in two adjacent domains. The polarized vectors for PFM identification in the (110) plane are $\mathbf{P}_{a-y}$ and $\mathbf{P}_{b-y}$, while axis *y* is perpendicular to tip motion. If one polarized vector is along the cantilever, it will not be detected, for instance, *x*-components $\mathbf{P}_{a-x}$ and $\mathbf{P}_{b-x}$ of $\mathbf{P}_a$ and $\mathbf{P}_b$. The phenomenon can be explained by the PFM working mechanism shown as vertical and torsional double-direction dark-cyan arrows in Figure 1b. The cantilever can collect OP polarized vectors by the vertical vibration, as well as identify the IP polarizations via cantilever torsional motion. As described in Figure 1c, instead of $\mathbf{P}_a$ and $\mathbf{P}_b$, $\mathbf{P}_{a-y}$ and $\mathbf{P}_{b-y}$ are captured in the phase channel ($\Delta\varphi = 180°$), assuming that $\mathbf{P}_a$ and $\mathbf{P}_b$ lie in the first and fourth quadrants, respectively. When the sample is rotated clockwise by 90°, $\mathbf{P}_a$ and $\mathbf{P}_b$ are moved to the fourth

DOI: 10.1021/acs.jpcc.7b03325
J. Phys. Chem. C 2017, 121, 14322−14329

and third quadrants. Corresponding y-components, $\mathbf{P}'_{a-y}$ and $\mathbf{P}'_{b-y}$, are in-phase ($\Delta\varphi = 0$). Under this circumstance, only one vector signal can be identified in the phase image. Thus, the interfacial polarization orientations can be determined by rotating sample.

3.2. Raman Spectra Analysis. The KNN-LN crystal has a purely orthorhombic structure analyzed by X-ray diffraction (XRD) at RT. Previous work on $LiNbO_3$-modified $(K_{0.5}Na_{0.5})NbO_3$ indicated that it possesses a giant piezoelectric coefficient d_{33} (189 pC/N), a high T_C (421 °C), and T_{O-T} (179 °C) by dielectric permittivity measurements.[31] Some attempts have been made to study the interactions of domain formation and the structural internal modes of the NbO_6 octahedron between O and T phases via Raman scattering experiments at RT.[14,24] In this case, NbO_6 octahedron vibration modes are composed of $1A_{1g}(\nu_1) + 1E_g(\nu_2) + 2F_{1u}(\nu_2, \nu_4) + 1F_{2g}(\nu_5) + 1F_{2u}(\nu_6)$. Among these modes, $1A_{1g}(\nu_1) + 1E_g(\nu_2) + 1F_{1u}(\nu_3)$ are the stretching modes, and others are the bending modes. Especially, for KNN-LN crystals, relatively strong scattering signals, symmetrical mode $A_{1g}(\nu_1)$, and antisymmetrical mode $F_{2g}(\nu_5)$ are detected, owing to an almost exquisitely symmetric structure of NbO_6 octahedron. As given in Figure 2a, Raman spectra exhibit a successive phase transition from O to T, and then to the cubic (C) phase at a temperature range 20−450 °C. In the heating cycle, the O−T phase transition occurs at 175−180 °C, and the peak shifts to higher frequency. While in the cooling process, T−O conversion in the scope of 165 and 175 °C can be found from Raman spectra. The clear hysteresis nature in adjacent phases, the thermal hysteresis effect, indicates that the O−T transition belongs to ferroelectric first-order phase transition in KNN-LN. A comparable study on KNN confirms that the rhombohedral−orthorhombic (R−O) phase transition delays almost 60 °C, and the O−T transition hysteresis is about 15 °C.[34] Except for the finding of the O−T−C phase transition, in a comparison of the scattering peaks in the O phase before heating (20 °C) with that after cooling procedure (20 °C), clear differences can be seen, in particular in the wavenumber ranges 200−300 and 550−650 cm^{-1}. In order to facilitate the explanation of this phenomenon and understand the correlation of interior structural changes and domain evolution, Raman spectra were fitted with several Lorentzian peaks in the frequency range between 200 and 800 cm^{-1}, magnified in Figure 2b,c, and they were associated with the main stretching modes $A_{1g}(\nu_1)$ and $E_g(\nu_2)$, as well as the bending mode $F_{2g}(\nu_5)$ of the NbO_6 octahedron. The center positions and full width of half maximums (FWHMs) of the vibrations are shown in Table 1.

For simplicity, the states are, respectively, defined as "state I" at 20 °C before heating, and "state II" at 20 °C after the cooling cycle, illustrated in Figure 2a. Interfacial polarization orientations in the O phase of KNN-LN correspond to the oxygen octahedron distortion along the face diagonals of the original cubic structure, which are considered as the orthorhombic lattice axes. There are 12 possible polarization vectors, which seem to form 60°, 90°, 120°, and 180° domain boundaries. The birth mechanism of 60°/90° domain walls is discussed as follows, on the basis of interior structural stress and bonding strength of the crystal, which is inspired from the crystal preparation conditions of cooling rate.[24] The non-180° domain-wall formation is able to release the internal stress applied to the NbO_6 octahedron, and lead to the decrease of bonding strength in a single crystal. The bonding strength of crystal lattices is directly analyzed by the center positions and FWHMs of Raman peaks (see Table 1). The density of non-180° domain boundaries can be estimated by comparing the wavenumber shifts from Raman spectra. After the cooling cycle, $A_{1g}(\nu_1)$ shifts from 600.7 to 628.8 cm^{-1}, and one of the $F_{2g}(\nu_5)$ modes shifts from 270.6 to 281.6 cm^{-1}. The modes $E_g(\nu_2)$ and separated $F_{2g}(\nu_5)$ are at 568.6 and 235.2 cm^{-1}, respectively, which represent the structural deformation distorted by 60° domain boundary formation.[24] Therefore, there is an increase in state II of bonding strength because of the shortening distance between Nb ions and coordinated O ions in the oxygen octahedron. Meanwhile, distorted NbO_6 units of 60° domain walls are attributed to different internal stresses.

On the basis of previous studies, it can be summarized that the similar sizes between nano-polar regions and ferroelectric domains generated the aggrandizement of internal stress caused by the structural phase transition.[35] Upon the ferroelectric phase transition, the renewed domain structures experience nucleation, growth, and combination of new domain nuclei. With consideration of single crystal growth together, when the nuclei generated from a solution of raw materials flux were grown, the extensional stress was produced external of the unit cell. In order to compensate for extensional stress, compressive stress emerged synchronously at the center of cell. The extensional stress is released during the nuclei combination process. The high density of the 90° domain wall in state I corresponds to the smaller size of the domain nucleus, which leads to weaker internal stress.[24] The 90° domain walls were detected in two types of a−c-90° (Figure 3) and IP a-90° domain walls (Figure 4). The results are in accordance with those from *in situ* Raman spectra, which indicate the larger bonding strength in state II than that in state I in the O phase. On the other hand, the formation of 60° domain wall can efficiently release the compressive stress produced from the center of the crystal. It is difficult to form 60° domain walls in state I due to the small compressive stress after the quenching and heating process. More 90° domain walls cause extensional stress to be released. In contrast, when the temperature reaches the T_{T-O} in the cooling cycle, larger domain nuclei lead to the decrease of the 90° domain-wall density and increase of the 60° domain-wall density, associated with the enlargement of bonding strength in the KNN-LN single crystal. Thus, general qualitative trends for the correlation between bonding strength and the density of the non-180° domain wall are summarized in Figure 2d. Absolute intensity or number of bonding strength and domain-wall density can be ignored owing to the unquantifiable conditions. Higher frequency shift and the reconstruction of a spontaneous polarized direction accompany the O−T phase transition, which leads to the larger bonding strength and more 90° domain walls in the T phase in the

Table 1. Center Positions and Full-Widths at Half-Maximums of Main Vibrational Modes in State I and State II Obtained from Raman Spectra in Figure 2

	state I (20 °C)		state II (20 °C)	
mode	FWHM (cm^{-1})	center (cm^{-1})	FWHM (cm^{-1})	center (cm^{-1})
$A_{1g}(\nu_1)$	37.8	600.8	32.2	628.8
$E_g(\nu_2)$			24.2	568.6
$F_{2g}(\nu_5)$	42.4	245.1	25.3	266.4
	18.0	270.6	21.2	281.6
[separated $F_{2g}(\nu_5)$]			35.1	235.2

DOI: 10.1021/acs.jpcc.7b03325
J. Phys. Chem. C 2017, 121, 14322−14329

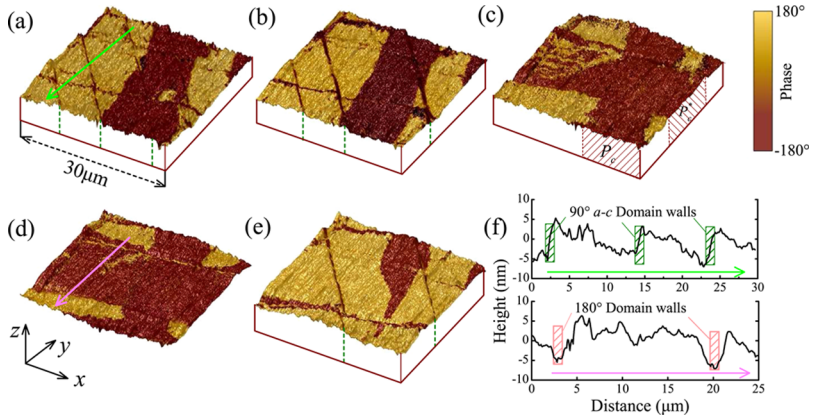

Figure 3. Three-dimensional topographies covered by their OP phase images of the KNN-LN crystal at (a) 20, (b) 160, (c) 180, (d) 240 °C when heating, and (e) 20 °C after cooling. All scan sizes are 30 μm. (f) Height profiles (line section) across crystal surfaces in parts associated with the 3D topographies. The locations of 90° a−c-domain walls are identified with green dotted lines in parts a, b, and e.

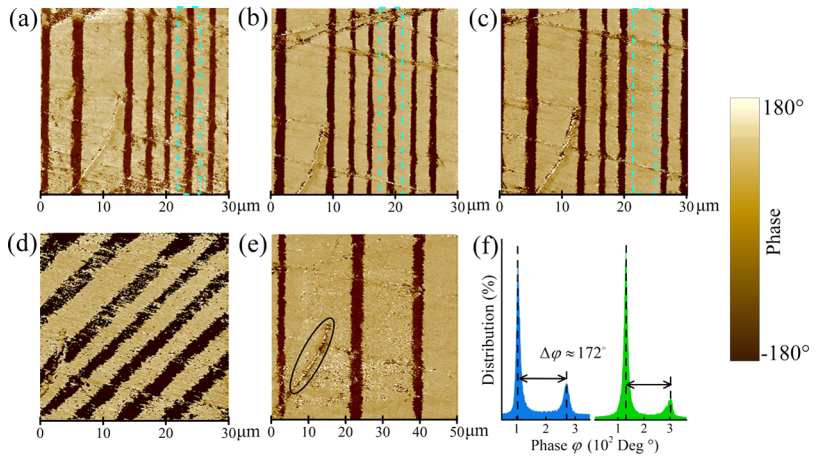

Figure 4. IP phase images of a KNN-LN single crystal at (a) 20, (b) 160, (c) 175, and (d) 200 °C when heating, as well as (e) 20 °C after cooling. (f) Depth analysis of phase channels corresponding to panel c in blue and d in green. The phase contrasts $\Delta\varphi$ (peak to peak distance) are about 172°. All scales are depicted.

KNN-LN crystal. In view of these results, we can ensure that Raman-active optical modes (ν_1, ν_2, ν_5) are sensitive to the relationship between structural information and the evolution of 60°/90° domain walls.

3.3. Surface Topography and *a*- and *c*-Domain Observation. As shown in Figure 3, temperature dependent PFM was used to investigate the evolution of surface topographies and domain structures accompanying the O−T phase transition. Figure 3a−e depicts surface topographies with coverage of their OP phase images in three-dimensional (3D) viewing during the cycles of heating and cooling from 20 to 240 °C. The scanning direction of the AFM tip is along axis x. In many ferroelectric crystal such as $PbTiO_3$ and $BaTiO_3$, 90° a−c-domain walls induce changes of the surface bending angles, further contributing to clear surface undulations.[36,37] A similar phenomenon can also be seen first in the KNN-LN single crystal. In a comparison of *in situ* height profile in 20 °C (Figure 3a) with that in 240 °C (Figure 3d) by line section analysis on 3D topographies shown in Figure 3f, the obvious changes of surface corrugations demonstrate that 90° a−c-domain walls (marked by green dotted lines) vanish with the progression from the O to the T phase. When the temperature decreases from 240 °C to RT, the 90° a−c-domain boundaries reappear. Likewise, there is no apparent difference of OP domains from 20 to 160 °C. However, across the O−T phase transition, vertical polarization reversal (stripe-like) is found with the width of ∼18 μm, denoted by P_c^*. In the T phase, illustrated in Figure 3c,d, c-domain nucleation and nuclei combination are observed in the zone of newly formed polarization (P_c^*). In addition, thermal expansion or contraction is quadratic to the first-harmonic ac field, and hence can be excluded by lock-in amplifier of PFM in the first harmonic. Reversible abrupt changes between O and T phases in domain patterns also illustrate that the effect of thermal expansion can be ignored. During the cooling cycle from the T to O phase, domain evolution is revealed including the reciprocal 180° c-domain and 90° a−c-domain walls. However, the striped c-domain (P_c) becomes narrow, as seen in a comparison of parts a and e of Figure 3. In addition, according to the surface corrugations, this can educe that the density of 90° a−c-domain wall after cooling (state II) is less than that before heating (state I). The result indicates that the larger internal stress in state II corresponds to the low density of the 90° domain wall in great accordance with Raman spectra.

With the discussion on obtaining the interfacial polarized angle aforementioned in Figure 1c, 90° in-plane domain walls are detected in Figure 4a−e. A black ellipse with a crescent shape in panel e marks the *in situ* scanning during the heating

DOI: 10.1021/acs.jpcc.7b03325
J. Phys. Chem. C 2017, 121, 14322−14329

and cooling procedures. To better clarify the *a*-domain evolution, another measured site that presents well-distributed striped *a*-domains was chosen. Depth analysis on phase distributions in Figure 4f confirms that the phase contrast $\Delta\varphi$ among different domains is approximately 172° associating with Figure 4c,d. With temperature increasing from 20 to 175 °C (Figure 4a–c), there is no great evolution of IP phases, whereas around 175 °C, one of the striped domains disappears as indicated by dotted rectangles. This may result from the unstable intermediate state during the O–T phase transition. Upon converting to the T phase, the direction of spontaneous polarization will be along one of the cube edges of the pseudocubic lattice, which is changed from one of the face diagonals in original orthorhombic pseudocubic structures. It directly leads to IP 90° domain boundary reconstruction at 200 °C (Figure 4d). Then, the crystal was cooled down to RT. The number of striped domain walls in Figure 4e (20 °C, scan size: 50 μm) is smaller than that in Figure 4a (20 °C, scan size: 30 μm). Therefore, together with the 90° *a*–*c*-domain evolution from Figure 3, it can be concluded that the density of 90° domain walls becomes reduced. The reduction in density after the thermal procedure also verifies the higher shifts of the Raman peaks, which indirectly indicate the strong internal stress applied to NbO_6 unit cells. In other words, with the O–T–O successive phase transition, it is worth mentioning that the results of Raman data are in good agreement with the evolution of 90° domain walls.

Taking 90° *a*–*c*/*a*–*a* and 180° *c*-domain walls into account, we summarize their evolutions during the thermal cycle into Figure 5 based on the direct observation by AFM/PFM above. From top to bottom, indicating the O–T–O phase transition, *c*-domain and *a*–*c*-domain-wall evolution can be seen in the left of the figure, as well as the 90° *a*–*a*-domain in the right. According to the experimental results, we have successfully explored the correlation between domain walls and the ferroelectric single crystal's interior stresses. However, other possible factors for thermal-induced stress and domain evolutions are still worth considering. Examples follow.

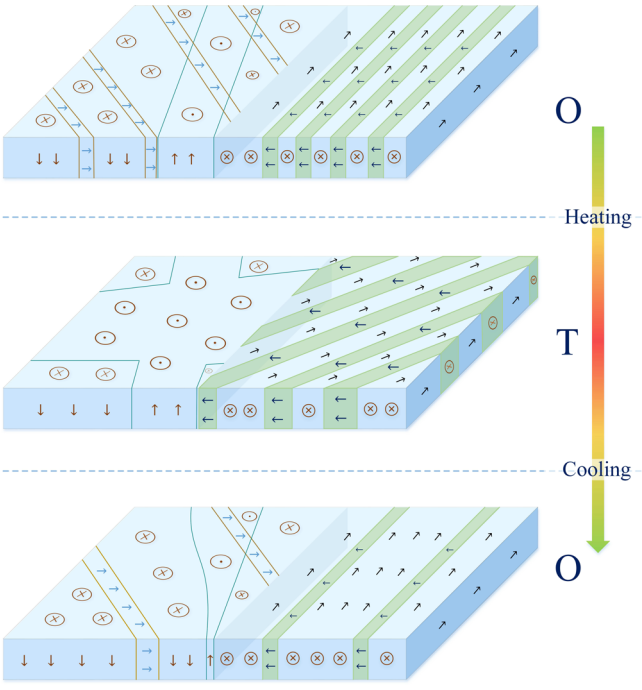

Figure 5. Schematic representation of domain evolution accompanied by O–T–O phase transition for a KNN-LN single crystal during a thermal cycle. All arrows indicate the model directions of polar axes.

(1) When a structural transition occurs, how do the structural defects of the single crystal exert influences on ferroelectric domain evolution, for instance, twinning and dislocations?

(2) Considering domain-wall energy transfer and depolarization contributions, why can it be concluded that domain evolution including the change of domain-wall density is directly linked with structural transformation?

On one hand, the main reasons why a KNN single crystal from the flux-Bridgman method holds the big internal stresses are listed here: (1) The nonuniform distribution of the thermal field in the growth furnace leads to the generation of thermal stress. (2) Due to the effects of raw materials and fabrication conditions, structural defects exist and give rise to the structural stress. (3) When undergoing the change from a paraelectric to a ferroelectric phase with decreasing temperature, the formation of ferroelectric domain leads to lattice mismatch which forms mechanical stress near the phase boundary.[31] On the basis of the phonon vibrational modes' discussion from Raman spectra, the extensional and compressive stresses, which are equivalent to the bonding strength in the KNN-LN crystal, efficiently represent these three types of stresses.[15]

On the other hand, importantly, it is well-known that the multidomain structure in ferroelectrics is formed according to the requirement of energy minimization. Depolarization field ($\mathbf{E}_d$), internal strain ($\mathbf{x}$), and phase change heat (ΔQ) should be taken into account with the presence and evolution of spontaneous polarization. First, assuming that the change of spontaneous polarization during phase transition is ΔP_s, depolarization field and energy (W_d) are given as

$$|\mathbf{E}_d| = -\frac{L\Delta P_S}{\varepsilon_0} \tag{1}$$

$$W_d = \frac{2.71P^2dV}{\varepsilon_0 t[1 + (\varepsilon_x\varepsilon_z)^{1/2}]} \quad (t \gg d) \tag{2}$$

where L is the depolarization factor ($0 < L < 1$); t is the sample thickness; d is domain width; V is bulk volume; and ε_0, ε_x, ε_z are the dielectric constants.[38] Thus, from the expressions, forming 180° domain walls can be of benefit to decrease W_d, which is proportional to the width of the domain. Similar research has revealed that one of ways to reduce strain energy is to generate 90° domain walls (or other non-180° domain boundaries).[39] It may be predicted on the basis of domain-wall energy that domain-wall generation with small spontaneous structural strain in the crystal is not in favor of reducing strain energy. According to the theory of mechanical twinning, a 90° domain is instantaneous when strain $\mathbf{x}$ meets the following requirement: $x^I < |\mathbf{x}| < x^{II}$, where x^I and x^{II} are two elastic limitations in the ferroelectric crystal.[40] In terms of the O–T first-order phase transition in KNN-LN, tetragonal and orthorhombic structures coexist near the phase boundary. The domain growth in a new phase is associated with the motion of the phase boundary. Supposing that KNN-LN holds a small internal strain, an instantaneous 90° domain will fade away with O–T phase boundary movement. This hypothesis is obviously false. For strain $|\mathbf{x}| > x^{II}$, a 90° domain wall is permanent and stable. Therefore, with large internal structural strain, the increase of

DOI: 10.1021/acs.jpcc.7b03325
J. Phys. Chem. C 2017, 121, 14322–14329

the 90° domain-wall density in the T phase is efficient for internal strain reduction when the KNN crystal goes through from the O to the T phase. In addition, the heat ΔQ of the phase transition plays a valuable role in domain formation during the structural transformation for the ferroelectric crystal of large ΔQ and high carrier concentration. However, domain evolution is not sensitive to ΔQ change for some ferroelectrics such as $BaTiO_3$ and $KTa_xNb_{1-x}O_3$.[41] It could not be considered that the heats of phase transition have contributions to 60°/90°/180° domain-walls' evolution in the KNN-LN single crystal.

Taking the above together, we have built the connection between the discussed complex internal strain system including thermal, structural, or mechanical stresses and the Raman spectra in KNN-LN crystal and domain-wall evolution. According to the system energy minimization for domain formation, decreasing depolarization energy and strain reduction during O−T transition are followed by the increase of non-180°/180° domain wall. Therefore, the mechanism of forming domain greatly matches *in situ* experimental results.

4. CONCLUSIONS

In summary, *in situ* characterizations of Raman spectra and PFM were used to investigate the 180°/non-180° domain evolution and structural transformation between O and T phases in a KNN-LN single crystal. Vibrational modes from Raman peaks are sensitive to the change of 60°/90° domain boundary density. In continuous heating and cooling cycles within a temperature range 20−240 °C, the increase of 60° domain wall and the decrease of 90° domain wall can be effectively distinguished by Raman-active optical modes, particularly $A_{1g}(\nu_1)$, $E_g(\nu_2)$, and the separated $F_{2g}(\nu_5)$. With the O−T−O successive transition, irreversible changes in density and reversible pattern of 90° *a*−*c*/*a*−*a*-domain boundary evolutions were presented clearly. The descent in density of the 90° domain wall was explained by the enhancement of internal stress and bonding strength which was obtained by higher frequency shifts of Raman peaks. In total, the results successfully demonstrate thermal stability of domain evolution in O and T phases. However, ferroelectric domain walls have to reorganize when the structure transfers between the O and T phases in a KNN-LN single crystal. It will promote the development of the domain-wall dependent nanodevices in the atmosphere of various temperatures.

AUTHOR INFORMATION

Corresponding Author

*Phone: +86-21-54345150. Fax: +86-21-54345119. E-mail: zghu@ee.ecnu.edu.cn.

ORCID

Zhigao Hu: 0000-0003-0575-2191

Author Contributions

The manuscript was written through contributions of all authors. All authors have given approval to the final version of the manuscript.

Notes

The authors declare no competing financial interest.

ACKNOWLEDGMENTS

This work was financially supported by Major State Basic Research Development Program of China (Grant Nos. 2013CB922300), Natural Science Foundation of China (Grant Nos. 61674057, 11374097, 61376129, 61504156, and 61227902), Projects of Science and Technology Commission of Shanghai Municipality (Grant Nos. 15JC1401600 and 14XD1401500), and the Program for Professor of Special Appointment (Eastern Scholar) at Shanghai Institutions of Higher Learning. In addition, authors wish to express our gratitude to Wei Hua (Tongji University, Shanghai) for his contributions on design of Figure 1.

REFERENCES

(1) Scott, J. F.; Paz de Araujo, C. A. Ferroelectric Memories. *Science* **1989**, *246*, 1400−1405.

(2) Rana, D. S.; Kawayama, I.; Mavani, K.; Takahashi, K.; Murakami, H.; Tonouchi, M. Understanding the Nature of Ultrafast Polarization Dynamics of Ferroelectric Memory in the Multiferroic $BiFeO_3$. *Adv. Mater.* **2009**, *21*, 2881−2885.

(3) Scott, J. F. Applications of Modern Ferroelectrics. *Science* **2007**, *315*, 954−959.

(4) McGilly, L. J.; Yudin, P.; Feigl, L.; Tagantsev, A. K.; Setter, N. Controlling Domain Wall Motion in Ferroelectric Thin Films. *Nat. Nanotechnol.* **2015**, *10*, 145−150.

(5) Cruz, M. P.; Chu, Y. H.; Zhang, J. X.; Yang, P. L.; Zavaliche, F.; He, Q.; Shafer, P.; Chen, L. Q.; Ramesh, R. Strain Control of Domain-Wall Stability in Epitaxial $BiFeO_3$ (110) Films. *Phys. Rev. Lett.* **2007**, *99*, 217601.

(6) Rubio-Marcos, F.; Del Campo, A.; Marchet, P.; Fernández, J. F. Ferroelectric Domain Wall Motion Induced by Polarized Light. *Nat. Commun.* **2015**, *6*, 6594.

(7) Xu, R.; Liu, S.; Grinberg, I.; Karthik, J.; Damodaran, A. R.; Rappe, A. M.; Martin, L. W. Ferroelectric Polarization Reversal via Successive Ferroelastic Transitions. *Nat. Mater.* **2014**, *14*, 79−86.

(8) Baghizadeh, A.; Vieira, J. M.; Gonçalves, J. N.; Willinger, M.-G.; Ferro, M. C.; Amaral, V. S. Nanodomains Coupled to Ferroelectric Domains Induced by Lattice Distortion in Self-Doped $LuMnxO_{3\pm\delta}$ Hexagonal Ceramics. *J. Phys. Chem. C* **2016**, *120*, 21897−21904.

(9) Bellou, A.; Bahr, D. F. Complementary Characterization Techniques for Identification of Ferroelectric Domains in $KNbO_3$ Single Crystals. *Mater. Charact.* **2008**, *59*, 688−692.

(10) Deng, H.; Zhang, H.; Zhao, X.; Chen, C.; Wang, X.; Li, X.; Lin, D.; Ren, B.; Jiao, J.; Luo, H. Direct Observation of Monoclinic Ferroelectric Phase and Domain Switching Process in $(K_{0.25}Na_{0.75})$-NbO_3 Single Crystals. *CrystEngComm* **2015**, *17*, 2872−2877.

(11) Qin, Y.; Zhang, J.; Yao, W.; Lu, C.; Zhang, S. Domain Configuration and Thermal Stability of $(K_{0.48}Na_{0.52})$ $(Nb_{0.96}Sb_{0.04})O_3$-$Bi_{0.50}(Na_{0.82}K_{0.18})_{0.50}ZrO_3$ Piezoceramics with High d_{33} Coefficient. *ACS Appl. Mater. Interfaces* **2016**, *8*, 7257−7265.

(12) Grüner, D.; Shen, Z. Direct Scanning Electron Microscopy Imaging of Ferroelectric Domains After Ion Milling. *J. Am. Ceram. Soc.* **2010**, *93*, 48−50.

(13) Rojac, T.; Ursic, H.; Bencan, A.; Malic, B.; Damjanovic, D. Mobile Domain Walls as a Bridge Between Nanoscale Conductivity and Macroscopic Electromechanical Response. *Adv. Funct. Mater.* **2015**, *25*, 2099−2108.

(14) Rubio-Marcos, F.; Del Campo, A.; López-Juárez, R.; Romero, J. J.; Fernández, J. F. High Spatial Resolution Structure of $(K,Na)NbO_3$ Lead-Free Ferroelectric Domains. *J. Mater. Chem.* **2012**, *22*, 9714−9720.

(15) Bortolani, F.; Del Campo, A.; Fernandez, J. F.; Clemens, F.; Rubio-Marcos, F. High Strain in $(K,Na)NbO_3$-Based Lead-Free Piezoelectric Fibers. *Chem. Mater.* **2014**, *26*, 3838−3848.

(16) Gao, J.; Hu, X.; Liu, Y.; Wang, Y.; Ke, X.; Wang, D.; Zhong, L.; Ren, X. Ferroelectric Domain Walls Approaching Morphotropic Phase Boundary. *J. Phys. Chem. C* **2017**, *121*, 2243−2250.

(17) Guo, Y.; Kakimoto, K.-i.; Ohsato, H. Phase Transitional Behavior and Piezoelectric Properties of $(Na_{0.5}K_{0.5})NbO_3CLiNbO_3$ Ceramics. *Appl. Phys. Lett.* **2004**, *85*, 4121.

(18) Bah, M.; Giovannelli, F.; Retoux, R.; Bustillo, J.; Clezio, E. L.; Monot-Laffez, I. Crystal Growth and Piezoelectric Properties of Lead-

DOI: 10.1021/acs.jpcc.7b03325
J. Phys. Chem. C 2017, 121, 14322−14329

free Based $K_{0.5}Na_{0.5}NbO_3$ by the Floating Zone Method. *Cryst. Growth Des.* **2016**, *16*, 315−324.
(19) Wang, K.; Yao, F. Z.; Jo, W.; Gobeljic, D.; Shvartsman, V. V.; Lupascu, D. C.; Li, J. F.; Rödel, J. Temperature-Insensitive (K,Na)NbO_3-Based Lead-Free Piezoactuator Ceramics. *Adv. Funct. Mater.* **2013**, *23*, 4079−4086.
(20) Saito, Y.; Takao, H.; Tani, T.; Nonoyama, T.; Takatori, K.; Homma, T.; Nagaya, T.; Nakamura, M. Lead-Free Piezoceramics. *Nature* **2004**, *432*, 84−87.
(21) Deng, Q. L.; Zhang, J. Z.; Huang, T.; Xu, L. P.; Jiang, K.; Li, Y. W.; Hu, Z. G.; Chu, J. H. Optoelectronic Properties and Polar Nano-Domain Behavior of Sol-Gel Derived $K_{0.5}Na_{0.5}Nb_{1-x}Mn_xO_{3-\delta}$ Nanocrystalline Films with Enhanced Ferroelectricity. *J. Mater. Chem. C* **2015**, *3*, 8225−8234.
(22) Tian, H.; Hu, C.; Meng, X.; Tan, P.; Zhou, Z.; Li, J.; Yang, B. Top-Seeded Solution Growth and Properties of $K_{1-x}Na_xNbO_3$ Crystals. *Cryst. Growth Des.* **2015**, *15*, 1180−1185.
(23) Wang, K.; Li, J. F. Domain Engineering of Lead-Free Li-Modified (K,Na)NbO_3 Polycrystals with Highly Enhanced Piezoelectricity. *Adv. Funct. Mater.* **2010**, *20*, 1924−1929.
(24) Inagaki, Y.; Kakimoto, K.-i.; Kagomiya, I. Ferroelectric Domain Characterization of Orthorhombic Sodium-Potassium Niobate Piezoelectric Crystals. *J. Am. Ceram. Soc.* **2010**, *93*, 4061−4065.
(25) Wang, X.; Wu, J.; Xiao, D.; Zhu, J.; Cheng, X.; Zheng, T.; Zhang, B.; Lou, X.; Wang, X. Giant Piezoelectricity in Potassium-Sodium Niobate Lead-Free Ceramics. *J. Am. Chem. Soc.* **2014**, *136*, 2905−2910.
(26) Wang, X.; Wu, J.; Xiao, D.; Cheng, X.; Zheng, T.; Zhang, B.; Lou, X.; Zhu, J. Large d_{33} in (K,Na) (Nb,Ta,Sb)O_3-(Bi,Na,K)ZrO_3 Lead-Free Ceramics. *J. Mater. Chem. A* **2014**, *2*, 4122−4125.
(27) Xu, L. P.; Jiang, K.; Zhang, J. Z.; Xu, G. S.; Hu, Z. G.; Chu, J. H. Phase Transitions and Thermotropic Phase Boundaries in MnO_2-doped $(K_{0.5}Na_{0.5})NbO_3$-0.05$LiNbO_3$ Single Crystals: Raman Scattering Evidence at Elevated Temperatures. *Appl. Phys. Lett.* **2015**, *106*, 122901.
(28) Yao, F. Z.; Wang, K.; Jo, W.; Webber, K. G.; Comyn, T. P.; Ding, J. X.; Xu, B.; Cheng, L. Q.; Zheng, M. P.; Hou, Y. D.; et al. Diffused Phase Transition Boosts Thermal Stability of High-Performance Lead-Free Piezoelectrics. *Adv. Funct. Mater.* **2016**, *26*, 1217−1224.
(29) Zheng, L.; Huo, X.; Wang, R.; Wang, J.; Jiang, W.; Cao, W. Large Size Lead-free (Na,K) (Nb,Ta)O_3 Piezoelectric Single Crystal: Growth and Full Tensor Properties. *CrystEngComm* **2013**, *15*, 7718.
(30) Liu, H.; Veber, P.; Koruza, J.; Rytz, D.; Josse, M.; Rödel, J.; Maglione, M. Influence of Ta^{5+} Content on the Crystallographic Structure and Electrical Properties of $[001]_{PC}$-Oriented (Li,Na,K) (Nb,Ta)O_3 Single Crystals. *CrystEngComm* **2016**, *18*, 2081−2088.
(31) Liu, Y.; Xu, G.; Liu, J.; Yang, D.; Chen, X. Dielectric, Piezoelectric Properties of MnO_2-doped $(K_{0.5}Na_{0.5})NbO_3$-0.05$LiNbO_3$ Crystal Grown by Flux-Bridgman Method. *J. Alloys Compd.* **2014**, *603*, 95−99.
(32) Zavaliche, F.; Yang, S. Y.; Zhao, T.; Chu, Y. H.; Cruz, M. P.; Eom, C. B.; Ramesh, R. Multiferroic $BiFeO_3$ Films: Domain Structure and Polarization Dynamics. *Phase Transitions* **2006**, *79*, 991−1017.
(33) Desmarais, J.; Ihlefeld, J. F.; Heeg, T.; Schubert, J.; Schlom, D. G.; Huey, B. D. Mapping and Statistics of Ferroelectric Domain Boundary Angles and Types. *Appl. Phys. Lett.* **2011**, *99*, 162902.
(34) Trodahl, H. J.; Klein, N.; Damjanovic, D.; Setter, N.; Ludbrook, B.; Rytz, D.; Kuball, M. Raman Spectroscopy of (K,Na)NbO_3 and $(K,Na)_{1-x}Li_xNbO_3$. *Appl. Phys. Lett.* **2008**, *93*, 262901.
(35) Okino, H.; Sakamoto, J.; Yamamoto, T. Cooling-Rate-Dependence of Dielectric Constant and Domain Structures in (1-x)$Pb(Mg_{1/3}Nb_{2/3})O_3$-x$PbTiO_3$ Single Crystals. *Jpn. J. Appl. Phys.* **2005**, *44*, 7160−7164.
(36) Wang, Y. G.; Dec, J.; Kleemann, W. Study on Surface and Domain Structures of $PbTiO_3$ Crystals by Atomic Force Microscopy. *J. Appl. Phys.* **1998**, *84*, 6795.
(37) Kalinin, S. V.; Bonnell, D. A. Temperature Dependence of Polarization and Charge Dynamics on the $BaTiO_3$ (100) Surface by Scanning Probe Microscopy. *Appl. Phys. Lett.* **2001**, *78*, 1116.
(38) Mitsui, T.; Furuichi, J. Domain Structure of Rochelle Salt and KH_2PO_4. *Phys. Rev.* **1953**, *90*, 193.
(39) Cahn, R. W. Twinned crystals. *Adv. Phys.* **1954**, *3*, 363.
(40) Garber, R. I. The Mechanism of Calcite and Nitre Twining under Plastic Deformation. *J. Phys. (Paris)* **1947**, *19*, 7.
(41) Fesenko, E. G.; Martynenko, M. Phase Transition and Formation of Domain Structure in Lead Titanate Crystals. *Izv. Akad. Nauk. SSSR, Ser. Fiz.* **1975**, *39*, 762−765.

DOI: 10.1021/acs.jpcc.7b03325
J. Phys. Chem. C 2017, 121, 14322−14329